Article

Not peer-reviewed version

Characterisation of Al-alloy EN AW-5454

Matjaž Balant , Tomaž Vuherer , Peter Majerič , Rebeka Rudolf *

Posted Date: 28 August 2024

doi: 10.20944/preprints202408.1989.v1

Keywords: Al alloy EN AW-5454; characterisation; microstructure; properties

Article

Characterisation of Al-Alloy EN AW-5454

Matjaž Balant [1], Tomaž Vuherer [2], Peter Majerič [2,3] and Rebeka Rudolf [2,3,4,*]

[1] Starkom d.o.o. A Mercedes Benz Group AG Company, Maribor, Slovenia
[2] University of Maribor, Faculty of Mechanical Engineering, Slovenia
[3] Zlatarna Celje d.o.o., Slovenia
[4] Pomurje Science and Innovation Centre, Murska Sobota, Slovenia
* Correspondence: R.R. - rebeka.rudolf@um.si

Abstract: A complementary characterisation of the Al-alloy EN AW-5454 was carried out, intended for obtaining the laser hybrid welding parameters of sub-assemblies in the automotive industry. The investigation included a microstructural examination, and determination of the alloy's properties using several analytical methods (HV5 hardness measurement, tensile test, Charpy impact toughness, fracture mechanics analysis). Samples were prepared in the longitudinal and transverse directions of a cold-rolled sheet of EN AW-5454 with thicknesses of 3.5 mm and 4 mm. The measured hardness on the thinner sheet was 5% higher than on the thicker sheet. The tensile and yield strength were nominal, while the elongations were smaller by 2.2 - 3.2% for the longitudinal samples and by 2.7 - 13.7% for the transverse samples. The smaller deviations from the nominal values are for the thinner sheet metal. A precise topographical analysis showed brittle fractures of the samples. The Charpy impact toughness results on the thicker plate showed a 20% greater work needed to break it in the longitudinal direction than in the transverse direction. With the thinner sheet metal, 40% greater work was needed. SEM (Scanning Electron Microscope) analysis has shown that the intermetallic $Al_6(Mn,Fe)$ particles in the longitudinal samples were mostly intact, with evidence of tough areas on the upper part of the fracture, indicating a better toughness than the specimens in the transverse direction. More crushed intermetallic particles were observed at the fractures of the transverse samples, and their distribution appeared to be more oriented in the direction of rolling. Fracture mechanics SENB (single edge notch bending) tests and their analysis showed that the resistance of the material to crack propagation in the longitudinal sample was about 50% greater than that in the transverse sample. SEM analysis of the fractures showed that the state of the intermetallic particles in the fracture mechanics testing, and the fracture mechanism differed from the one in the Charpy fractures.

Keywords: Al alloy EN AW-5454; characterisation; microstructure; properties

1. Introduction

It is known from the literature that the most important properties of the Al-alloy EN AW-5454 are its excellent corrosion resistance, good formability [1] and weldability [2]. The Al-alloy EN AW-5454 also has a good ratio of density and load-bearing capacity [3,4], excellent deformation properties [5–7], and is, therefore, very suitable for use in the automotive industry. This is particularly important for reducing the weight of the product, which affects its LCA (Life Cycle Assessment) significantly, thereby improving the environmental footprint [8] of the product, as it results in lower energy consumption for vehicle engines [9]. The basic properties of the Al-alloy EN AW-5454 are important for further use in the automotive industry, as they must be considered when designing a product that is installed in a vehicle. The properties of the Al-alloy EN AW-5454 depend on the basic microstructure, so it is very important to evaluate the microstructure and all the key microstructural elements that affect the properties of the final assembly during subsequent processing, finishing or joining of the Al-product with other sub-assemblies first. Laser hybrid welding is recognised as a promising joining process [10], as it compensates for the shortcomings of the laser and arc welding processes when used properly. It is introduced in the field of Al-alloy welding, where the practices

 doi:10.20944/preprints202408.1989.v1

and optimal technological parameters are unknown. The development is in the experimental phase of determining the optimal conditions for each structural element and for each Al-alloy separately. When choosing optimal parameters, laser hybrid welding offers many advantages [11], as it is much faster and more productive than classical arc welding [12], ensures lower energy input [13–15] into the weld joint, and thus changes the microstructure in the HAZ (heat affected zone) [16–18], residual internal stresses [19] and related deformations, since Al-alloys have high temperature expansions and contractions [20], enables a wider tolerance of the welding gap [21], ensures a better appearance of the welded joints and reduces the welding defects [22,23]. In laser hybrid welding, the transformation of the intermetallic phase, base and eutectic phases, will probably occur in the region of the weld joint, due to the locally high energy input, remelting of the alloy and mixing of the melt with the added welding material [1,5,7,24,25], which will need to be investigated in more detail in further practical tests.

The purpose of the research task was to characterise the delivered sheet metal of two thicknesses made from the Al-alloy EN AW-5454, and to determine in detail whether the mechanical properties are affected by the microstructural elements discovered in the previous research [26]. The results of this research will later be used to determine the optimal welding parameters of laser hybrid welding, observing whether the intermetallic phase tends to establish equilibrium, and whether the intermetallic phase dissolves during laser hybrid welding, or remains in the same form as in the base material. By determining the optimal welding parameters, we will try to avoid errors that can occur in the weld joint as much as possible, and, at the same time, preserve the best possible properties of the base material.

2. Materials and Methods

2.1. Materials

For the investigation we used materials supplied by the manufacturer Speira GmbH (Grevenbroich, Germany). Sheet strips made of cold-rolled Al-sheets of two thicknesses (3.5 mm and 4 mm), width 856 mm, were supplied, which were cut to a length of 1000 mm in the supplied condition O (soft) [27].

The nominal chemical composition of the supplied Al-alloy EN AW-5454-D used for the tests and analyses is listed in Table 1.

Table 1. The nominal chemical composition of the Al-alloy EN AW-5454-D (in wt.%).

Thickness [mm]	Element	Si	Fe	Cu	Mn	Mg	Cr	Zn	Ti	Al
	Minimum	-	-	-	0.5	2.6	0.05	-	-	Rest
	Maximum	0.25	0.4	0.1	1.0	3.0	0.2	0.2	0.05	
3.5		0.16	0.31	0.06	0.79	2.86	0.07	0.03	0.02	95,70
4.0		0.18	0.32	0.05	0.76	2.85	0.05	0.04	0.02	95,73

2.2. Sample Preparation

All the samples for the conducted investigation were taken from the central parts of the delivered sheet metal in a width of 300 mm, as shown in the sampling scheme in Figure 1. According to the same scheme, the samples were taken from both sheet thicknesses. The samples were labelled according to Table 2.

Preprints.org (www.preprints.org) | NOT PEER-REVIEWED | Posted: 28 August 2024 doi:10.20944/preprints202408.1989.v1

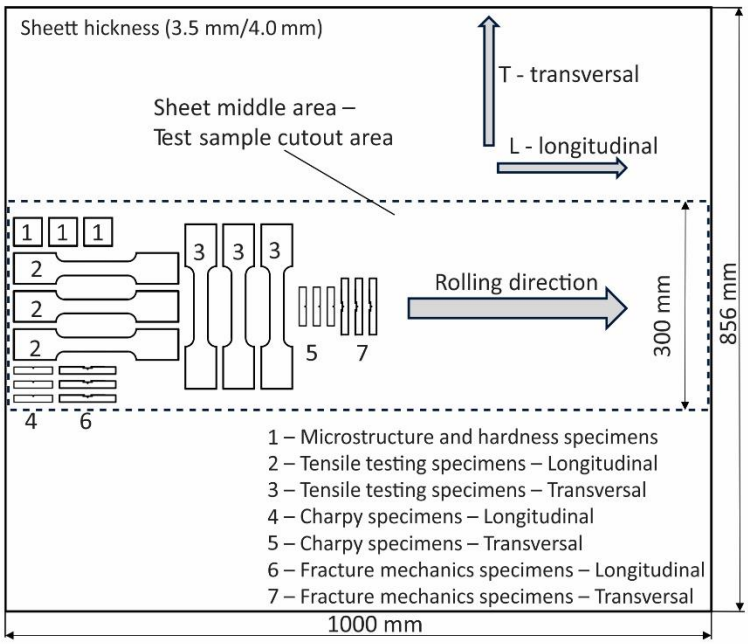

Figure 1. The scheme of taking samples from the delivered sheet metal.

Table 2. Specimen naming for different tests.

Test	Thickness [mm]	Direction	Specimen	Thickness [mm]	Direction	Specimen
Hardness	4.0	L	ALH1, ALH2, ALH3	3.5	L	BLH1, BLH2,
Tensile testing	4.0	L	ALT1, ALT2, ALT3	3.5	L	BLT1, BLT2,
	4.0	T	ATT1, ATT2, ATT2	3.5	T	BTT1, BTT2,
Charpy	4.0	L	ALC1, ALC2, ALC3	3.5	L	BLC1, BLC2,
	4.0	T	ATC1, ATC2, ATC3	3.5	T	BTC1, BTC2,
Fracture mechanics	4.0	L	ALF1, ALF2, ALF3	3.5	L	BLF1, BLF2,
	4.0	T	ATF1, ATF2, ATF3	3.5	T	BTF1, BTF2,

Designation of the specimen:

-First letter: A-thickness 4 mm; B- thickness 3.5 mm;

-Second letter: L-Longitudinal; T-Transversal;

-Third letter: H-Hardness t.; T-Tensile t.; C-Charpy; F-Fracture mech.

-Number: Specimen Nr.

2.2.1. Metallographic Sample Preparation

For the microstructural characterisation, three samples with dimensions of 15x30 mm were prepared, taken in the longitudinal direction for each sheet thickness. The samples were embedded with Bakelite mass, and prepared according to the procedure described in Table 3. The naming of the samples is defined in Table 2 (the samples for hardness measurements):

- ALH1, ALH2, ALH3
- BLH1, BLH2, BLH3

Table 3. Technological parameters of polishing.

Polishing agent	Load [N]	Rotational speed [rpm]	Direction of rotation	Time [min:s]
P600 sandpaper	20	300/30	Same direction	5:00

 doi:10.20944/preprints202408.1989.v1

9 µm diamond suspension + lubricant	20	150/30	Opposite direction	5:00
3 µm diamond suspension + lubricant	20	150/30	Same direction	4:00
1 µm diamond suspension + lubricant	20	150/30	Same direction	2:30
0.06 µm colloidal silica + lubricant	20	150/30	Opposite direction	2:00

After completion of the individual grinding/polishing steps, the sample was washed with running water. This was followed by cleaning in an ultrasonic bath in ethanol for 5 minutes and drying with dry air. After the final polishing with colloidal silica, the sample was cleaned in an ultrasonic bath for 20 min. This was followed by a process of chemical etching of the polished surface of the sample, which was carried out with an etchant (H_2O: HF = 10:1). The etching times varied from 10 s to several minutes.

2.2.2. Sample Preparation for the Hardness Measurements

The samples prepared for microstructure analysis were later used to measure the hardness of HV5. The naming of the samples was in accordance with Table 2:

- ALH1, ALH2, ALH3
- BLH1, BLH2, BLH3

2.2.3. Sample Preparation for the Tensile Testing

Three test specimens were produced for each testing, in accordance with the recommendations of the ISO 6892 - 1 Standard. The dimensions of the test specimens are shown in Figure 2. They were taken as shown in Figure 1. The naming of the samples was in accordance with Table 2:

- ALT1, ALT2, ALT3
- ATT1, ATT2, ATT3
- BLT1, BLT2, BLT3
- BTT1, BTT2, BTT3

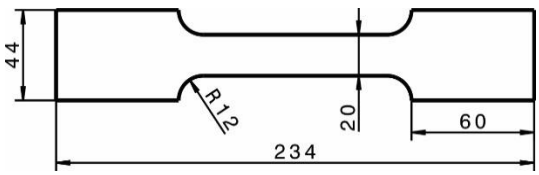

Figure 2. Specimen dimensions for tensile testing.

2.2.4. Sample Preparation for the Charpy Impact Toughness Tests

The geometry of the Charpy test specimens was adapted to the thickness of the material, and is shown in Figure 3. The test specimens were produced with an ISO–V notch across the entire thickness of the material. The ISO-V notch depth was 2 mm. The samples were taken from both sheet thicknesses, as shown in Figure 1, and named according to Table 2:

- ALC1, ALC2, ALC3
- ATC1, ATC2, ATC3
- BLC1, BLC2, BLC3
- BTC1, BTC2, BTC3

Preprints.org (www.preprints.org) | NOT PEER-REVIEWED | Posted: 28 August 2024 doi:10.20944/preprints202408.1989.v1

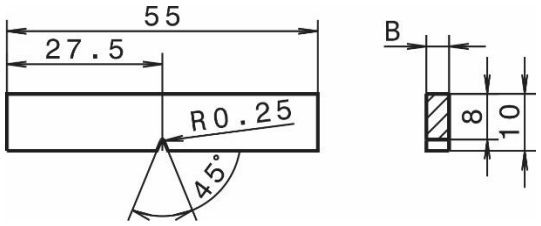

Figure 3. Specimen dimensions for the Charpy instrumental testing.

2.2.5. Sample Preparation for the Testing of Fracture Mechanics

The test pieces were made in two directions with respect to the rolling direction: longitudinal and transverse. The geometry of the fracture mechanics test specimens is shown in Figure 4. Laterally, along the wider side, the test specimens were sanded finely with 600 grit sandpaper. Lines were marked on both surfaces of the test specimens with a height marker, to monitor the controlled growth of the crack. In the middle of the test piece there was a groove for the CMOD sensor and a V notch. Three samples were made from each rolling direction, as follows (see the Table of all the material samples, Table 2):

- ALF1, ALF2, ALF3
- ATF1, ATF2, ATF3
- BLF1, BLF2, BLF3
- BTF1, BTF2, BTF3

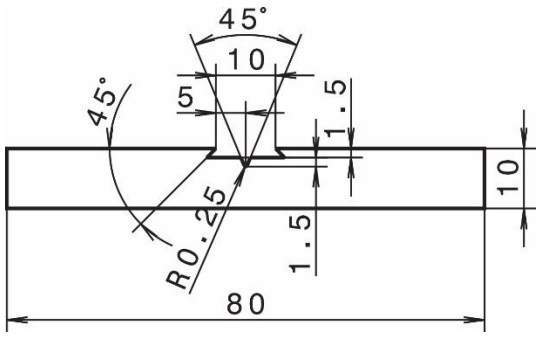

Figure 4. Specimen dimensions for the fracture mechanics tests.

2.3. Performing of Analyses and Testing

2.3.1. Microstructural Analysis

The microstructure of the selected sample was investigated with an optical metallographic microscope, NIKON Epiphot 300 (Japan), with an Olympus DP12 camera (Boston, USA). A Scanning Electron Microscope (SEM), Sirion 400NC (FEI, USA), with an Energy-Dispersive X-ray spectroscope INCA 350 (Oxford Instruments, UK), was used for the detailed microstructure observation and microchemical analyses of the different metallic phases found in the sample. The sample was analysed from secondary and backscattered electron images.

Analysis of the Fracture Surfaces

Examination of the fracture surfaces was performed with a Leica WILD M10 optical microscope with a Leica MC170 HD digital camera (Leica Microsystems GmbH, Germany). The fracture surfaces of the samples were examined:

- Tensile testing: ALT3, ATT2, BLT2 and BTT1;
- Charpy testing with labels: ALC1, ATC1, BLC1 and BTC1;
- Fracture mechanics with labels: ALF1, ALF2, ATF1 and ATF2, at the sites where the crack was initiated from the notch, and at fractures that were about 1 mm away from the notch.

 doi:10.20944/preprints202408.1989.v1

2.3.2. Hardness Measurements HV5

The hardness of the samples was examined with Vickers hardness measurements HV5 on a ZWICK 3212 machine (Ulm, Germany). The measurement load of 5 kg was selected for the given sample dimensions.

2.4. Determination of the Mechanical Properties

2.4.1. Tensile Testing

The tensile tests were performed on a Zwick/Roell Vibrophore 100 tensile testing machine. The elastic modulus E [GPa], tensile strength R_m [MPa], yield strength $R_{p0.2}$ [MPa] and elongation A_g [%] were measured using a quasi-static process without prestressing force. The Mean values and Standard Deviation were calculated for each specimen. The test specimens were previously settled at room temperature (20°C), where the tests were performed.

2.4.2. Instrumented Charpy Test

The instrumented Charpy test was performed according to the EN ISO 148-1 Standard [28], at room temperature on an AMSLER RPK 300 Charpy hammer with the computerised results recorded in an Excel file. During the impact test, time t [s], force F [N], displacement s [mm] and velocity v [m/s] of the impact hammer were recorded and stored digitally. The total energy for fracture E [J] was calculated, which was divided into the energy for crack initialisation E_i [J] and the energy for crack propagation E_p [J]. The average impact work was calculated for the fracture of the test piece with a V notch KV_{pov} [J/cm2].

2.4.3. Fracture Mechanics

The fracture mechanics tests were performed using the method in accordance with the ASTM E1820 Standard [29]. The tests were carried out in three steps:

Step 1: Initiating the pre-crack to the desired length by bending on a RUMUL Cractronic machine (pre-fatigue)

Step 2: Propagating a crack by bending in a tensile testing machine (Smitweld 1405 tensile machine)

Step 3: Post-fatigue RUMUL Cractronic machine (post-fatigue) and final breakage of the specimen

A CMOD sensor was placed in the groove of the SENB specimens to measure the displacement of the crack tip opening. During the test itself, the force was measured in a three-point bending test, where the mechanical notch was on the bottom side and the SENB test specimen was supported by two supports with a distance of 64 mm between them. During the test, the data were recorded and force F [N] – CMOD [mm] diagrams were drawn.

After the test post-fatigues were done to mark the stable crack growths after the SENB tests, which were followed until the SENB specimen's final fractures. The normalisation method according to the ASTM E1820 Standard [29] was used, to evaluate the SENB fracture mechanics test and to determine the resistance curve (J-integral - Δa).

3. Results and Discussion

3.1. Microstructure

The microstructure of the Al-alloy had already been analysed in a previous study [26], which showed that it consists of the main α-Al phase with dissolved Mg and Si, and, in some places, there is also the presence of a very fine eutectic Mg_2Si phase and an intermetallic phase $Al_6(Mn,Fe)$.

 doi:10.20944/preprints202408.1989.v1

3.2. Hardness Measurements

The HV5 hardness was measured on the previously metallographically prepared samples [30]. From the HV5 results shown in Table 4, it can be seen that the HV5 average differed by approximately 5 %, which indicates the probable strengthening of the Al-alloy due to the rolling process [31] and subsequent cold forming. It is known that the AW 5454 alloy can only be hardened by kneading [32,33].

Table 4. The average of the HV5 hardness measurements on the cross-sections of the samples ALH and BLH.

Specimen thickness [mm]	Specimen	No. of measurements	Average sample hardness	Std. Deviation
4.0	ALH1	14	81.4	5.9
	ALH2	13	84.0	5.1
	ALH3	10	85.2	3.3
	Average	37	83.3	5.2
3.5	BLH1	12	87.6	5.6
	BLH2	16	85.9	5.9
	BLH3	16	88.4	5.9
	Average BLH	44	87.2	5.9

3.3. Tensile Testing

The tensile tests yielded the results shown in Figure 5 and summarised in Table 6.

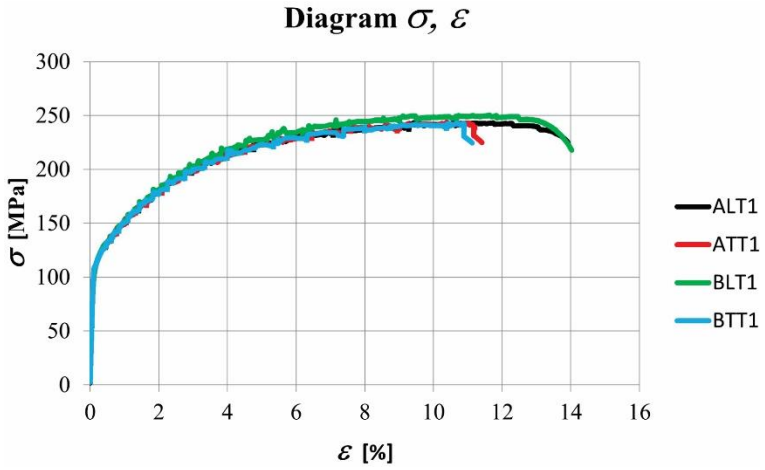

Figure 5. Diagrams of the tensile testing of specimens: ALT1 (black line); ATT1 (red line); BLT1 (green line); BTT1 (blue line).

The nominal mechanical properties of the materials for both delivered and used thicknesses defined from the manufacturer are listed in Table 5.

Table 5. Mechanical properties of the 3.5 mm and 4.0 mm thick Al-Sheets.

Nominal thickness [mm]		Thickness [mm]	R_m [MPa]	$R_{p0.2}$ [MPa]	*A80* [%]
4.0	Min.	3.94.1	220	90	18
	Max.		260	130	
	Meas.	3.96	240	105	20.3

 doi:10.20944/preprints202408.1989.v1

Nominal thickness [mm]		Thickness [mm]	R_m [MPa]	$R_{p0.2}$ [MPa]	*A80* [%]
3.5	Min.	3.4	220	90	18
	Max.	3.6	260	130	
	Meas.	3.47	240	105	20.2

Table 6. Tensile testing results.

Specimen thickness [mm]	Direction	Specimen	*E* [GPa]	R_m [MPa]	$R_{p0.2}$ [MPa]	A_g [%]
4.0	L	ALT1	70.42	250.2	118.6	16.26
		ALT2	71.99	250.5	117.9	17.02
		ALT3	71.22	249.6	117.8	19.02
		Average	71.54	250.1	118.1	17.43
		STD	0.33	0.34	0.33	1.16
	T	ATT1	70.01	243.6	116.9	14.73
		ATT2	70.99	243.5	116.7	15.89
		ATT3	70.01	243.2	115.3	15.97
		Average	70.34	243.4	116.3	15.53
		STD	0.46	0.17	0.72	0.56
3.5	L	BLT1	71.91	251.2	118.1	16.06
		BLT2	69.66	252.9	118.6	18.02
		BLT3	70.15	254.7	118.5	17.64
		Average	70.57	252.9	118.4	17.59
		STD	0.97	1.43	0.19	0.85
	T	BTT1	70.02	244.2	116,9	16.27
		BTT2	68.36	245.8	115.7	15.03
		BTT3	68.85	245.0	115.6	15.25
		Average	69.07	245.0	116.1	17.51
		STD	0.70	0.66	0.59	0.68

When comparing the nominal values with the measured values, it can be seen that the measured values for tensile and yield strength are in the area between the upper and lower nominal values, while the average measured elongations are smaller by 2.2 - 3.2% for the longitudinal samples and

 doi:10.20944/preprints202408.1989.v1

by 2.7 - 13.7% for the transverse samples. Smaller deviations from the nominal are noted for the thinner sheet metal. From the results of the performed tensile tests in Figure 5 and Table 6, we can understand the influence of the rolling direction of the material on the elongation and tensile strength of the material. In the case of longitudinal samples with thicker sheet metal, the elongation achieved was 11.5% higher than in the case of the transverse samples. With the thinner sheet metal, the elongation was only 0.7% greater. This is a consequence of the isotropy of the material due to rolling and the texture development [34–41]. The fracture surface analysis and 3D fracture topography were included to clarify Table 6 further.

The appearance of the fracture surface depends on the mechanism of the formation, growth and merging of microcavities. In the case of a ductile fracture, the surface relief is a set of small pits in which the particle where the pit formation begins is clearly visible. Micropits are formed in areas of localised interruption of the stress propagation, such as, e.g., a second phase particle, inclusion, grain boundary, or dislocation pile-up [42]. In the case of a brittle fracture, lamellae or steps are visible on the fracture surface, and the surface is smoother with less presence or absence of pits. A brittle fracture is a low-energy failure that propagates along well-defined low-index crystallographic planes known as cleavage planes. Al-alloys are polycrystalline, and contain grain boundaries, inclusions and dislocations. These defects affect fracture propagation, and change the fracture surface to some extent. Sometimes, microconstituents present in the crack path can cause the alloy specimen to exhibit a mixed fracture mode [42]. Additionally, we wanted to determine in detail whether the mechanical properties identified by the tensile test are affected by microstructural elements. Therefore, we performed a detailed topographical analysis of the fractures. Figure 6 shows the optical microscope macro images and 3D topographies of the tensile test fracture surfaces. From the investigation of the fractures, it is clear that none of the examined fractures shows a ductile fracture, but all the fractures are extremely brittle, as there are no visible features of a ductile fracture that would indicate a large deformation of the material. Minimal differences in the longitudinal and transverse directions are visible. In addition, the fracture surfaces of samples ALT3 and ATT2 were examined by SEM, and are shown in Figure 7. Figure 7a,c show the locations of the fractures examined on the samples by SEM. There is a visible difference between longitudinally and transversely rolled specimens. In the longitudinally rolled specimen in Figure 7b, a more ductile fracture was seen, which appears as smaller pits, in contrast to the transversely rolled specimen in Figure 7d, where a less ductile fracture is visible. At the fracture of the longitudinal sample ALT3, the particles of the intermetallic phase were more oriented, with fewer crushed particles. More ductile areas are visible, which indicates a more ductile fracture, and is also confirmed by the higher elongation values. Mixed shear-tension areas were seen (darker areas), where the ductile structure of the surface was discernible. At the fracture of the transverse sample ATT2, the particles of the intermetallic phase were not oriented clearly and looked like they were inserted into the surface, with more crushed particles than in the longitudinal samples. Fewer ductile regions are visible, indicating a more brittle fracture, and also confirmed by the lower elongation values. Particles of the intermetallic phase on which the fracture was initiated are present on all the fracture surfaces.

 doi:10.20944/preprints202408.1989.v1

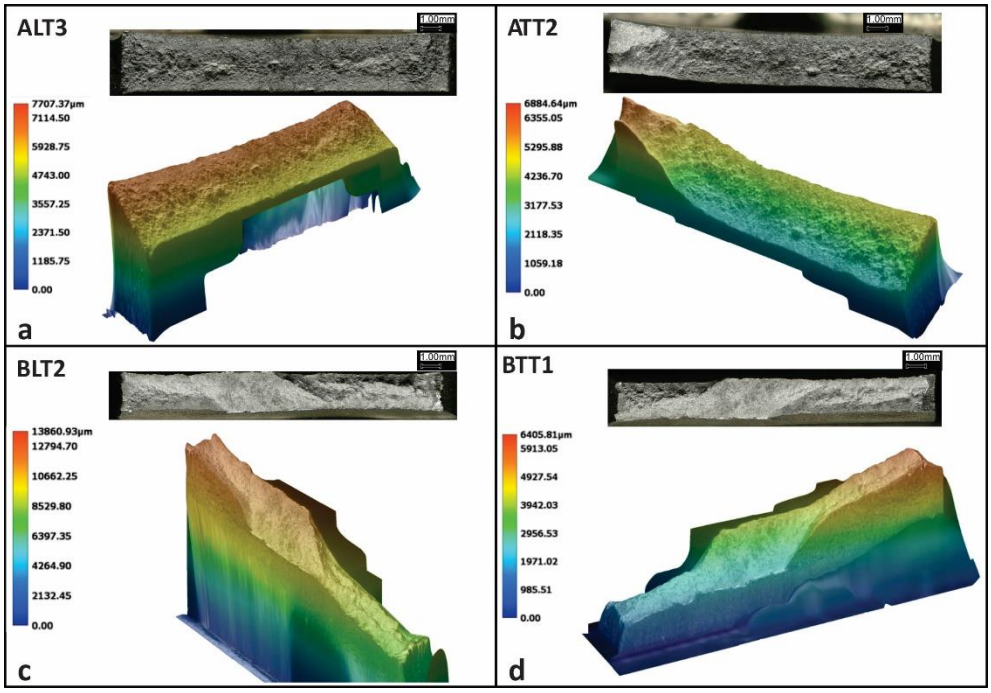

Figure 6. Fracture surface of the tensile testing - macro-optical picture and 3D Topography: a) Specimen ALT3; b) Specimen ATT2; c) Specimen BLT2; d) Specimen BTT1.

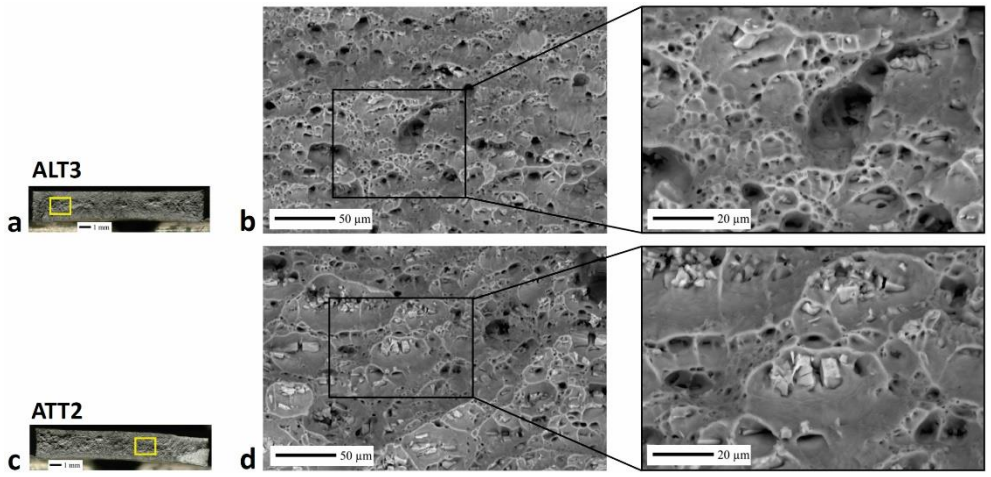

Figure 7. Fracture surface of the tensile testing - macro-optical picture and SEM pictures: **a)** and **b)** Specimen ALT3; **c)** and **d)** Specimen ATT2.

3.4. Charpy Testing Results

The results of the instrumented Charpy test are shown in Figure 8a–d, where the diagrams of the force are plotted as a function of time F – t and the total energy used for fracture as a function of time E – t. The left side of Figure 8 (Figures a and c) shows the results of the instrumented Charpy test on the 4 mm thick sheet, while the right side of Figure 8 (Figures b and d) shows the test results on the 3.5 mm thick sheet. The upper diagrams in Figure 8 (Figures a and b) show the test results on samples with a notch in the longitudinal direction of sheet metal rolling, and the lower diagrams in Figure 8 (Figures c and d) with a notch in the transverse direction of sheet metal rolling. It can be seen from the diagrams that the total energy required for the fracture of samples with a notch in the longitudinal direction (red lines) is greater than for the fracture of samples with a notch in the transverse direction. This is confirmed by the results in Table 7, where it can be seen that the average work required for a break in a thicker sheet in the longitudinal direction is more than 20% greater

 doi:10.20944/preprints202408.1989.v1

than the work required for a break in the transverse direction. An even bigger difference is noticeable with the thinner sheet metal, where the work required to break in the longitudinal direction was more than 40% greater than the work needed to break the specimen in the transverse direction. This is the result of pre-treatment of the metal sheet [31,34–41]. More precise results, where the total energy for fracture is also divided into the energy for initiation (E_i) and energy for propagation (E_p), are given in Table 7.

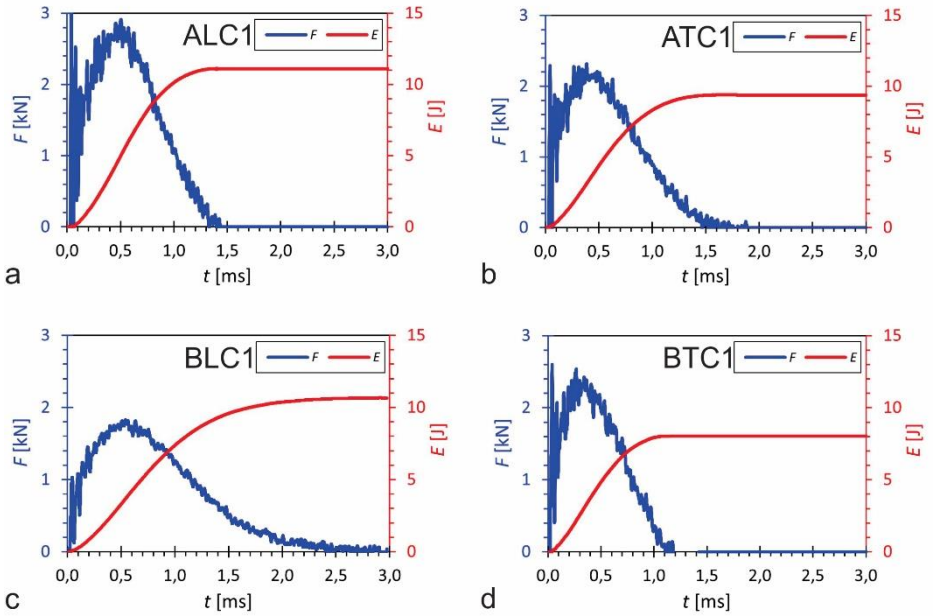

Figure 8. Results of the instrumented Charpy tests: a) Specimen ALC1; b) Specimen ATC1; d) Specimen BLC1; b) Specimen BTC1.

Table 7. Instrumental Charpy test results.

Specimen thickness [mm]	Direction	Sample	Impact energy E [J]	E_i [J]	E_p [J]	KV_{pov} [J/cm²]
4.0	L	ALC1	11.10	5.07	6.03	36.22
		ALC2	11.66	5.29	6.37	
	T	ATC1	9.37	3.88	5.49	30.16
		ATC2	9.51	3.24	6.27	
3.5	L	BLC1	10.66	3.87	6.79	38.73
		BLC2	10.54	4.46	6.08	
	T	BTC1	7.68	3.06	4.62	27.64
		BTC2	7.38	2.24	5.14	

The fractures where the crack started from the notches and the fractures that are about 1 mm away from the notches were inspected carefully. In the fractures of the longitudinal samples, it was observed that the intermetallic particles were mostly intact, but their distribution appeared random - non-oriented, due to the crosswise fracture with respect to the direction of rolling. On the upper part of the fracture (Figure 9a–f) ductile areas can be seen along the edges of the pits, which indicates a better toughness than the samples in the transverse direction. More crushed intermetallic particles were observed at the fractures of the transverse samples, and their distribution appeared to be more oriented in the direction of rolling. On the thinner material (3.5 mm), a linear orientation of the intermetallic phase particles was observed, due to the deeper rolling of the material. On the upper

 doi:10.20944/preprints202408.1989.v1

side of the fracture, where the fracture was initiated, larger intermetallic particles can be seen, while, lower down, these particles are smaller and more fragmented. In some places, tough areas can be seen between the larger pits. The particles of the intermetallic phase are of different sizes.

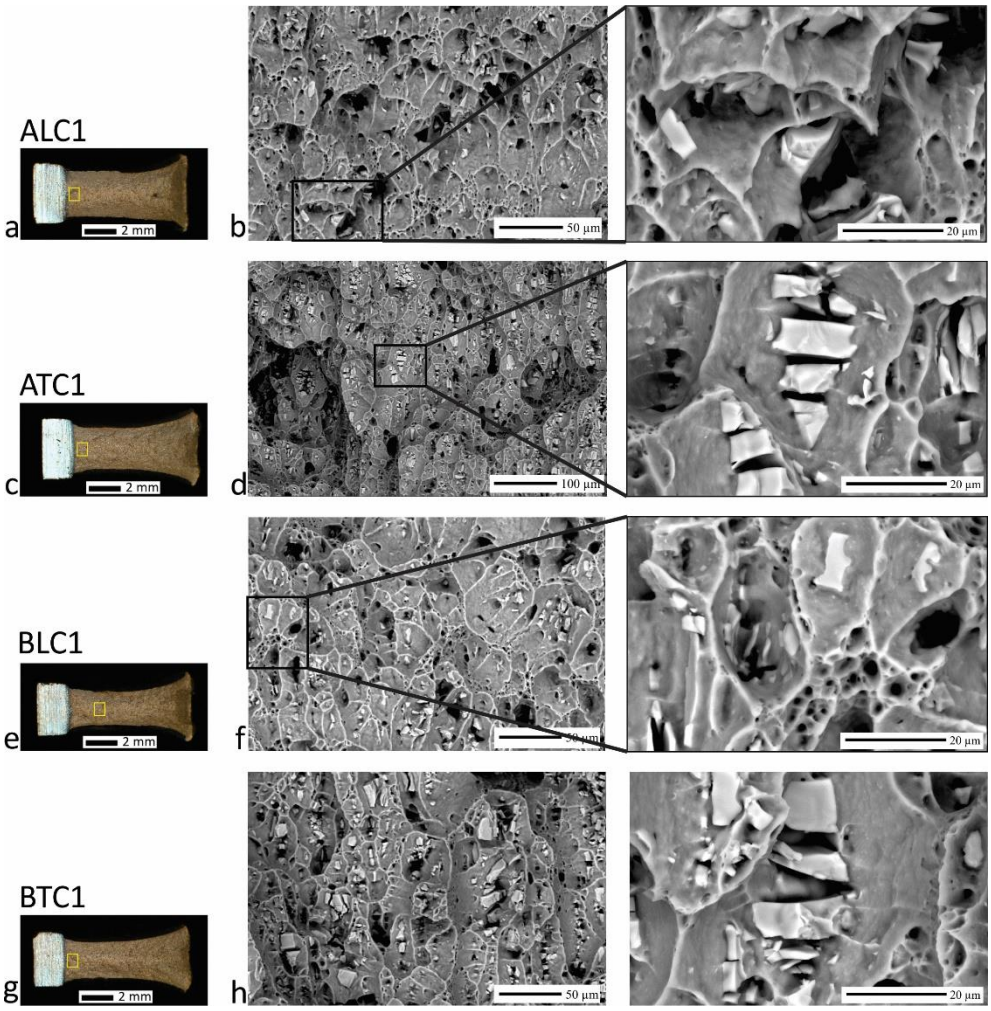

Figure 9. Fractured surfaces of the instrumented Charpy tests: a) Makro picture of specimen ALC1, b) SEM of specimen ALC1, c) Makro picture of specimen ATC1, d) SEM of specimen ATC1, e) Makro picture of specimen BLC1, f) SEM of specimen BLC1, g) Makro picture of specimen BTC1, h) SEM of specimen BTC1.

3.5. Results of the Fracture Mechanics

The force/CMOD (crack opening displacement) and resistance curves J - Δa were drawn, and are shown in Figure 10. In Figure 10a,b, the diagrams show the results for the longitudinally rolled specimen, while Figures 10 c and d show the results for a transversely rolled specimen. The green marks on the graph b and d are the experimental results, continued by a fitted curve according to the normalisation method.

All the SENB fractures of the test specimens are shown in Figure 11a,b, where the morphology of the fracture is indicated with marked initial cracks, stable crack growth and the final fracture. All the surfaces were analysed carefully by SEM. The images of the SEM analysis are shown in Figure 12a–f.

The critical value of the J integral (fracture toughness) J_{IC} was defined according to the ASTM E1820 Standard [29], as the intersection of the resistance curve J - Δa and the parallel of the construction line that intersects the x axis as the crack dulls Δa was 0.2 mm [29,42–46]. Then, it was extended and closed simultaneously. From the diagrams in Figure 10b,d we can see that the fracture toughness of the material n was about 50% higher in the longitudinally rolled sample.

 doi:10.20944/preprints202408.1989.v1

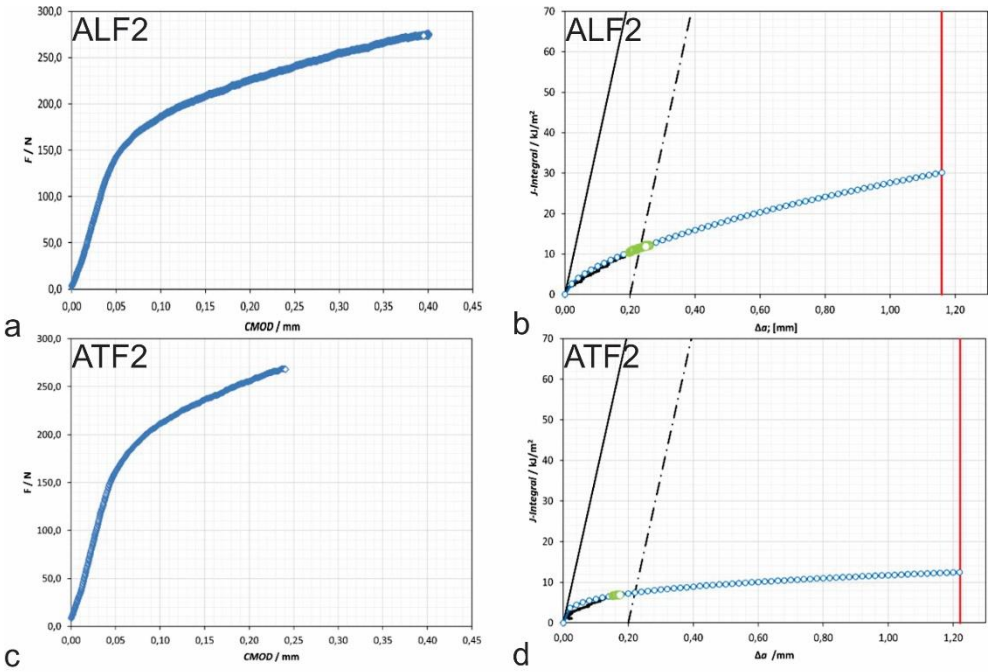

Figure 10. Force/CMOD (crack mouth opening displacement) plot of the test sample: a) ALF2, c) ATF2; J integral resistance curve of the test sample: b) ALF2 and d) ATF2.

Figure 11 shows different areas of crack growth, which are mutually delimited by the crack growth fronts. In Figures 11c and 11d the arrows indicate the different areas of fractures caused by different load regimes from the initial notch: a crack caused by pre-fatigue, where different fatigue parameters are used, a stable crack growth caused by a quasi-stationary force loading test, and a crack which was formed by fatigue after the experiment with the purpose of marking the crack. At the end, there was the final break of the sample. Crack initiation started in the middle of the specimen from a pre-fatigue crack. The crack progressed symmetrically with respect to the middle of the specimens. In the specimens in Figures 11 a and c, the length of stable crack growth is greater than in the specimens in Figures 11 b and d. The places of crack initiation were analysed with SEM in more detail, which are shown in Figure 12. Figures 12a, b and c show the place of crack initiation on the ALF2 sample, and Figures 12d, e and f show the place of crack initiation on the ATF2 sample at different magnifications. As in the fractures with the Charpy hammer, particles of the intermetallic phases $Al_6(Mn,Fe)$ were also noticeable on these fractures. EDX analysis was performed, to confirm the intermetallic phase, presented below.

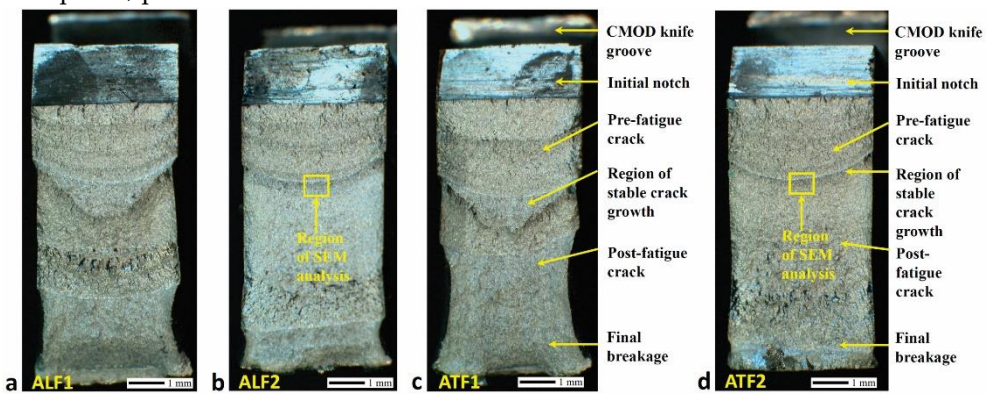

Figure 11. Fractured toughness specimen surfaces with fractographic detail – macro pictures: a) Specimen ALF1; b) Specimen ALF2; c) Specimen ATF1; d) Specimen ATF2.

Zhu et al. [24] investigated the formation mechanism of the intermetallic phase $Al_6(Mn,Fe)$ in the casting of Al-Mg alloys, where it was indicated that $Al_6(Mn,Fe)$ is the dominant metastable phase

 doi:10.20944/preprints202408.1989.v1

in contrast to the stable phase $Al_{13}(Mn,Fe)_4$. The experimental data of their research confirmed that the addition of Mn in the alloy inhibits the transformation of the metastable phase $Al_6(Mn,Fe)$ into the stable phase $Al_{13}(Mn,Fe)_4$ under non-equilibrium solidification conditions. Using EDS analysis of the precipitated particles, they discovered that the average Mn/Fe atomic ratio in the $Al_6(Mn,Fe)$ phase decreases as the Mn/Fe atomic ratio decreases in the melt. They also discovered that the $Al_6(Mn,Fe)$ phase grows to form two elongated prismatic morphologies: a rhombic prism and a rectangular prism. The primary phase, $Al_6(Mn,Fe)$, shows a hollow structure, and the eutectic phase is in the form of fine solid particles.

The presence of the intermetallic phase $Al_6(Mn,Fe)$ was also demonstrated in the research and simulations by Engler et al. [7]. The calculated composition of a typical Al-alloy AA5454 is shown in the Al-rich corner of the Al–Fe–Mn–Si–Mg phase diagram as a function of Mg.

The condition of the intermetallic particles at the fractures of the mechanical SENB test specimens differs from the previously described intermetallic particles of the Charpy hammer fractures. As we assumed that the properties of the material differ in different directions due to the anisotropy of the material, tests were carried out on specimens in the longitudinal and transverse directions with respect to the direction of rolling [47]. On the longitudinal samples, crushed particles of the second phase were visible, while, on the samples in the transverse direction, the particles of the second phase were mostly intact. Rolling during material fabrication created a stretched texture of oriented [34–40], compressed intermetallic particles, which were reduced by rolling [41]. The additional resistance of the intermetallic particles to crack growth in a longitudinally oriented pattern contributes energy that inhibits the crack effectively. In the cross-oriented sample with respect to the rolling, however, the crack mostly bypasses the intermetallic particles, and, therefore, this structure is more fragile.

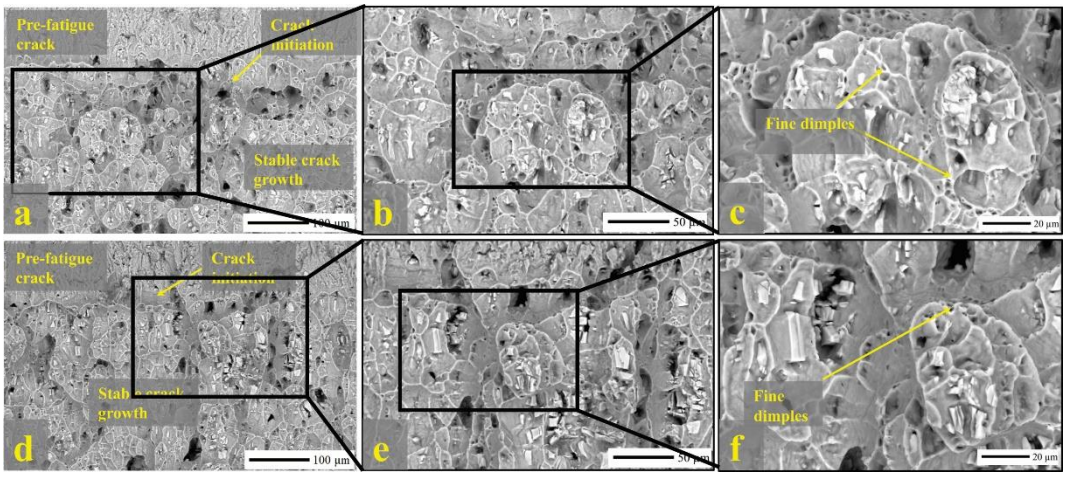

Figure 12. Fractured toughness specimen surfaces – SEM of specimen: a) to c) ALF2; d) to f) ATF2.

The SEM fracture images of the sample in the longitudinal direction are shown in Figures 12 a – c. Figures 12 d – f show the SEM fracture images of the sample in the transverse direction. The left Figures (a and d) show the areas of initial crack, crack initiation and stable crack growth. It can be seen from the images that there are more fine pits on the longitudinal samples, which indicates a tougher fracture and higher ductility than the samples in the transverse direction of rolling.

3.6. EDX Analysis of Sample Fracture Surfaces for Fracture Mechanics

EDX chemical analysis was performed on two samples, namely, on the ALF2 sample in the longitudinal direction and on the ATF2 sample in the transverse direction. Figure 13 shows the locations of the EDX analysis of the ALF2 sample (the SEM image capture location is marked in Figure 11b), and Figure 14 shows the locations of the EDX analysis of the ATF2 sample (the SEM image capture location is marked in Figure 11d). The normalised results of the EDX point analysis of selected sites or particles of the second phase are shown in Table 8 for the ALF2 sample and Table 9 for the ATF2 sample. Due to the surrounding Al-matrix, the size of the analysed particles and the

 doi:10.20944/preprints202408.1989.v1

nature of the analysis performed, the Al values are higher than the actual chemical composition of these particles [7]. In all the analysed sites of both samples the content of Mn and Fe is increased, which indicates particles of the intermetallic phase $Al_6(Mn,Fe)$ [1,5,24].

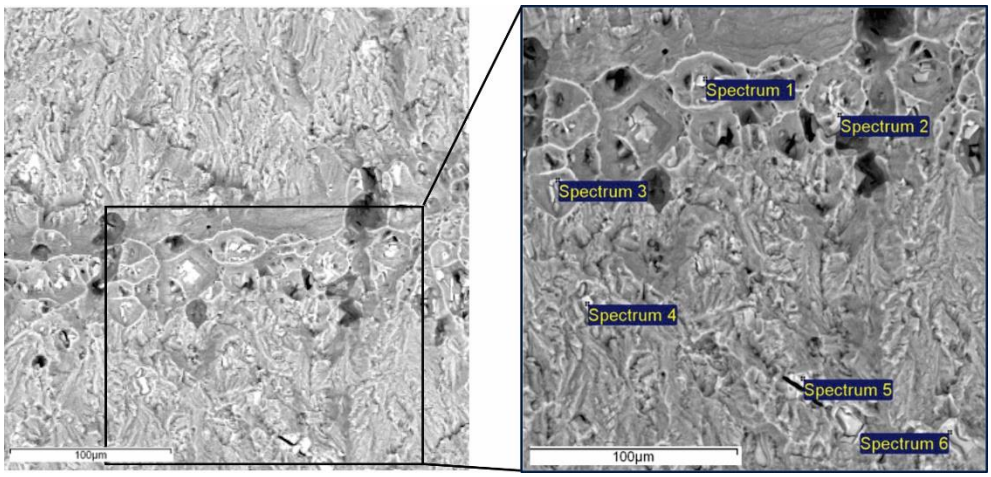

Figure 13. Marked areas of the EDX analysis of specimen ALF2.

Table 8. EDX analysis results of specimen ALF2 (in wt.%).

Spectrum	Mg	Al	Mn	Fe	Total
Spectrum 1	1.37	81.29	6.86	10.48	100
Spectrum 2	0.98	79.90	9.94	9.18	100
Spectrum 3	1.45	79.82	7.16	11.57	100
Spectrum 4	0.29	76.31	10.47	12.93	100
Spectrum 5	0.36	77.91	9.18	12.55	100
Spectrum 6	0.43	79.07	8.06	12.44	100
Mean	0.81	79.06	8.61	11.52	100
Std. Dev.	0.52	1.74	1.49	1.44	
Max.	1.45	81.29	10.47	12.93	
Min.	0.29	76.31	6.86	9.18	

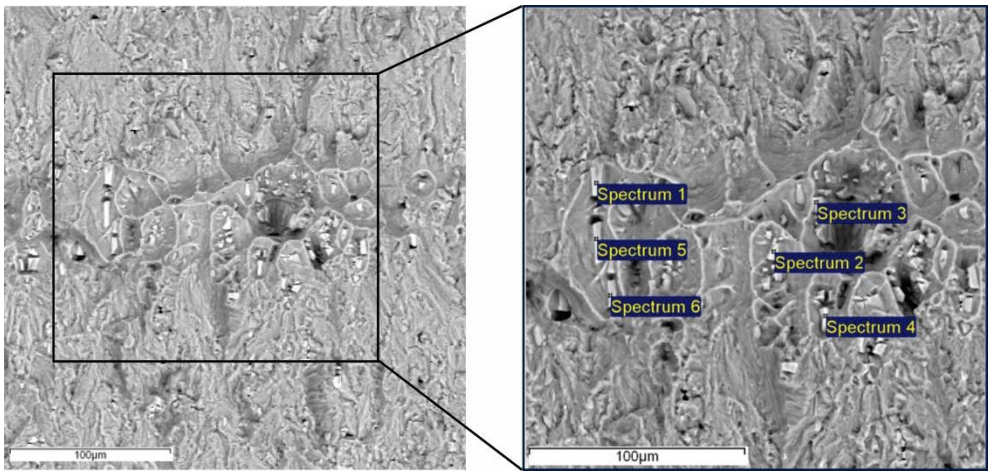

Figure 14. Marked areas of the EDX analysis of specimen ATF2.

 doi:10.20944/preprints202408.1989.v1

Table 9. EDX analysis results of specimen ATF2 (in wt.%).

Spectrum	Mg	Al	Mn	Fe	Total
Spectrum 1	0.61	77.90	8.70	12.79	100
Spectrum 2	0.49	73.62	9.32	16.57	100
Spectrum 3	0.30	79.15	7.93	12.62	100
Spectrum 4	0.33	68.63	13.92	17.12	100
Spectrum 5	0.66	74.52	9.54	15.28	100
Spectrum 6	1.45	53.54	18.10	26.91	100
Mean	0.64	71.23	11.25	16.88	100
Std. Dev.	0.42	9.41	3.95	5.26	
Max.	1.45	79.15	18.10	26.91	
Min.	0.64	71.23	11.25	16.88	

The revealed microstructure is practically single-phase as α-aluminium with more than 97.4 surface area, and Al_6(Mn, Fe) and Mg_2Si phases are also present [26]. The results of HV5 indicate that the Al-alloy surface is different in hardness, depending on the conditions of the previous mechanical processing. Research by Xiangzhen Zhu et al. showed that the Al_6(Mn,Fe) phase has different morphologies and sizes, which is a consequence of the Fe content [24]. Through tests and analyses, it was established that the orientation and distribution of the intermetallic phases affect the properties of the material significantly in relation to the direction of rolling. The thickness of the material also has an influence on the individual properties of the material. From the different modes of fracture (the tensile test compared to the Charpy impact test) and crack propagation, it can be seen that the intermetallic particles behave differently in terms of the mode and rate of deformation, or failure of the test specimens. In the tensile tests, crushed intermetallic particles were seen, while in the Charpy test these particles were crushed to a lesser extent, but mostly the intermetallic particles remained intact, due to the high rate of collapse. In the fracture-mechanical SENB tests, the intermetallic particles were crushed, due to the long impact on the material and resistance to crack growth. All the results of the performed tests indicate that the influence of the time of application of the external force is not negligible. Due to the different temporal action of the external force, the correct orientation of the particles of the intermetallic phase with respect to the direction of rolling is important.

The intermetallic phases listed above have an evident effect on the mechanical properties of the base material, depending on their orientation, so it is important to take this into account in the construction and production of transformed and welded parts [13], as this affects the properties of the final product. The Aluminium alloy EN AW-5454 belongs to the alloys that are hardened by kneading. With the input of energy during welding, the structure of the material loosens in the heat-affected area [5,7]. During the welding itself, it will be necessary to pay attention to the lowest possible energy input [14,48], in order to preserve the properties of the base material, but still sufficient to meet the load-bearing requirements of the welded joint. In further research, it will be necessary to pay attention to the heat-affected zone [18], the area of joining the filler and basic material [20] and the equiaxed grain zone (EGZ) [16]. It will also be important to avoid the occurrence of welding defects, as these have a significant impact on the load-bearing capacity and safety of welded joints [22].

4. Summary and Conclusions

A precise characterisation was performed of two Al-alloy EN AW-5454 metal sheets with thicknesses of 3.5 mm and 4 mm. The key findings of this characterisation are:

1. On average, the measured hardness on the thinner sheet was 5% higher than the measured hardness on the thicker sheet.

 doi:10.20944/preprints202408.1989.v1

2. In the tensile testing, the longitudinal elongation of the thicker sheet was 11.5% greater than the transverse, and the longitudinal elongation of the thinner sheet was 0.7% greater than the transverse.
3. None of the examined fractures were tough, rather, they were extremely brittle fractures.
4. In the Charpy tests the average work needed to break a thicker plate in the longitudinal direction was more than 20% greater than the work needed to break it in the transverse direction. In the case of the thinner sheet metal, the work required to break the specimen in the longitudinal direction was more than 40% greater than the work required to break the specimen in the transverse direction.
5. In the Charpy tests the intermetallic particles in the longitudinal samples were mostly intact, their distribution appeared random, and the upper part of the fracture showed tough areas along the edges of the pits, which indicates a better toughness than the tests in the transverse direction. More crushed intermetallic particles were observed at the fractures of the transverse samples, and their distribution appeared to be more oriented in the direction of rolling.
6. The critical size of the J_{IC} integral, as well as the fracture toughness of the longitudinally rolled SENB specimen, was about 50% greater than that of the transverse specimen. This was also confirmed by the higher resistance curve J - Δa.
7. The state of the intermetallic particles on the mechanical SENB fractured surfaces was different from the intermetallic particles in the Charpy hammer fractures. On the longitudinal samples the particles of the second phase were crushed, while the particles of the second phase on the samples in the transverse direction were mostly whole. The texture on the thinner sheet was stretched and oriented with more compressed intermetallic particles, which were smaller than on the thicker sheet.
8. Particle resistance to crack growth in the longitudinal SENB specimen contributed to the energy that inhibited the crack.
9. The performed EDX analysis showed an increased content of Mn and Fe at all the analysed points of the sample fracture surfaces, indicative for the intermetallic phase particles Al_6(Mn,Fe). The analysed microstructure was a single-phase α-alumina with present phases of Al_6(Mn, Fe) and Mg_2Si.

From the above findings, we can conclude that the thickness of the material and the direction of rolling affect the material properties of the Al-alloy significantly, due mainly to the size, shape, orientation and arrangement of the Al_6(Mn,Fe) intermetallic phase particles.

Author Contributions: "Conceptualization, M.B., T.V. and R.R.; methodology, M.B., T.V. and R.R.; software, P.M.; validation, T.V. and R.R.; formal analysis, T.V. and P.M.; investigation, M.B., T.V., P.M. and R.R.; resources, R.R.; data curation, P.M.; writing—original draft preparation, M.B., T.V., P.M. and R.R.; writing—review and editing, T.V. and R.R..; visualization, P.M.; supervision, R.R.; project administration, R.R.; funding acquisition, R.R. All authors have read and agreed to the published version of the manuscript."

Funding: The APC was funded by the Slovenian Research Agency (grant numbers, P2-0120 Research Programme).

Data Availability Statement: We encourage all authors of articles published in MDPI journals to share their research data.

Conflicts of Interest: The authors declare no conflicts of interest.

References

1. Salej Lah, A.; Vončina, M.; Paulin, I.; Medved, J.; Fajfar, P.; Volšak, D. THE INFLUENCE OF CHEMICAL COMPOSITION AND HEAT TREATMENT ON THE MECHANICAL PROPERTIES AND WORKABILITY OF THE ALUMINIUM ALLOY EN AW 5454. *Mater. Tehnol.* **2021**, *55*, doi:10.17222/mit.2021.155.
2. Volpone, L.M.; Mueller, S. Joints in light alloys today: the boundaries of possibility. *Weld. Int.* **2008**, *22*, 597–609, doi:10.1080/09507110802411518.
3. Sheng, K.; Lu, L.; Xiang, Y.; Ma, M.; Wu, Z. Crack behavior in Mg/Al alloy thin sheet during hot compound extrusion. *J. Magnes. Alloy.* **2019**, *7*, 717–724, doi:https://doi.org/10.1016/j.jma.2019.09.006.
4. Mikhaylovskaya, A. V; Portnoy, V.K.; Mochugovskiy, A.G.; Zadorozhnyy, M.Y.; Tabachkova, N.Y.; Golovin, I.S. Effect of homogenisation treatment on precipitation, recrystallisation and properties of Al –

3% Mg – TM alloys (TM=Mn, Cr, Zr). *Mater. Des.* **2016**, *109*, 197–208, doi:https://doi.org/10.1016/j.matdes.2016.07.010.
5. Engler, O.; Kuhnke, K.; Hasenclever, J. Development of intermetallic particles during solidification and homogenization of two AA 5xxx series Al-Mg alloys with different Mg contents. *J. Alloys Compd.* **2017**, *728*, 669–681, doi:https://doi.org/10.1016/j.jallcom.2017.09.060.
6. Hirsch, J. Aluminium Alloys for Automotive Application. *Mater. Sci. Forum - MATER SCI FORUM* **1997**, *242*, 33–50, doi:10.4028/www.scientific.net/MSF.242.33.
7. Engler, O.; Liu, Z.; Kuhnke, K. Impact of homogenization on particles in the Al–Mg–Mn alloy AA 5454 – Experiment and simulation. *J. Alloys Compd.* **2013**, *560*, 111–122, doi:https://doi.org/10.1016/j.jallcom.2013.01.163.
8. Hirsch, J.; Al-Samman, T. Superior light metals by texture engineering: Optimized aluminum and magnesium alloys for automotive applications. *Acta Mater.* **2013**, *61*, 818–843, doi:https://doi.org/10.1016/j.actamat.2012.10.044.
9. García Gutiérrez, I.; Elduque, D.; Pina, C.; Tobajas, R.; Javierre, C. Influence of the Composition on the Environmental Impact of a Casting Magnesium Alloy. *Sustainability* 2020, *12*.
10. Casalino, G.; Maso, U.; Angelastro, A.; Campanelli, S.L. Hybrid Laser Welding: A Review. *DAAAM Int. Sci. B.* **2010**, 413–430, doi:10.2507/daaam.scibook.2010.38.
11. Paul, C.; Nicolae, J. INDUSTRIAL APPLICATIONS FOR MSG - LASERHYBRID WELDING PROCESS. *Rev. Tehnol. Neconv.* **2011**, *15*.
12. Staufer, H. LaserHybrid welding for industrial applications. In Proceedings of the Proceedings of SPIE - The International Society for Optical Engineering; 2007; Let. 6346 PART.
13. *ISO/TR 18491:2015 (E) Welding and allied processes — Guidelines for measurement of welding energies*; 2015;
14. *Schweißen –Empfehlungen zum Schweißen metallischer Werkstoffe –Teil 1: Allgemeine Anleitungen für das Lichtbogenschweißen; Deutsche Fassung EN 1011-1*; 2009;
15. Leo, P.; Renna, G.; Casalino, G.; Olabi, A.G. Effect of power distribution on the weld quality during hybrid laser welding of an Al–Mg alloy. *Opt. Laser Technol.* **2015**, *73*, 118–126, doi:https://doi.org/10.1016/j.optlastec.2015.04.021.
16. Kostrivas, A.; Lippold, J.C. Fusion boundary microstructure evolution in aluminium alloys. *Weld. World* **2006**, *50*, 24–34, doi:10.1007/BF03263458.
17. Leo, P.; D'Ostuni, S.; Casalino, G. Hybrid welding of AA5754 annealed alloy: Role of post weld heat treatment on microstructure and mechanical properties. *Mater. Des.* **2016**, *90*, 777–786, doi:10.1016/j.matdes.2015.10.150.
18. Aleo, V. Effect of Welding on the Width of the Heat -Affected Zone of Aluminum Alloys, ProQuest Dissertations Publishing, 2004.
19. Çevik, B.; Gülenç, B. The effect of welding speed on mechanical and microstructural properties of 5754 Al (AlMg3) alloy joined by laser welding. *Mater. Res. Express* **2018**, *5*, 86520, doi:10.1088/2053-1591/aad3b0.
20. Courbière, M. Welding Aluminum Alloys. V *Metallurgy and Mechanics of Welding: Processes and Industrial Applications*; Elsevier Scopus, 2010; str. 433–471 ISBN 9781848210387.
21. Aalderink, B.J.; Pathiraj, B.; Aarts, R.G.K.M. Seam Gap Bridging of Laser Based Processes for the Welding of Aluminium Sheets for Industrial Applications. *Int. J. Adv. Manuf. Technol.* **2010**, *48* SE-*1*, 143–154, doi:10.1007/s00170-009-2270-x.
22. Katayama, S. Fundamentals and Details of Laser Welding 2020.
23. Ma, Y.R.; Cai, C.; Liu, Z.J.; Xie, J.; Yang, C. Plasma Monitoring During Laser-MIG Hybrid Welding Process Based on LabVIEW. *CHINESE J. LASERS-ZHONGGUO JIGUANG* **2022**, *49*, doi:10.3788/CJL202249.0202014.
24. Zhu, X.; Blake, P. The formation mechanism of Al6(Fe, Mn) phase in die-cast Al-Mg alloys. *CrystEngComm* **2018**, *20*, doi:10.1039/C8CE00675J.
25. Li, Y.J.; Arnberg, L. A eutectoid phase transformation for the primary intermetallic particle from Alm(Fe,Mn) to Al3(Fe,Mn) in AA5182 alloy. *Acta Mater.* **2004**, *52*, 2945–2952, doi:https://doi.org/10.1016/j.actamat.2004.02.041.
26. Balant, M.; Rudolf, R. Microstructure Characterization of Al-Alloy AW 5454 Intended for Ecological Laser Hybrid Welding. *Metall. Mater. Data* **2024**, *2*, 59–64, doi:10.30544/MMD30.
27. *EN 515:2017 Aluminium and aluminium alloys - Wrought products - Temper designations*; 2017;
28. EN ISO 148-1 Metallic materials – Charpy pendulum impact test – Part 1: Test method 2016.
29. ASTM E1820: Standard Test Method for Measurement of Fracture Toughness. *Astm* 2015, 1–54.
30. Broitman, E. Indentation Hardness Measurements at Macro-, Micro-, and Nanoscale: A Critical Overview. *Tribol. Lett.* **2016**, *65*, 23, doi:10.1007/s11249-016-0805-5.
31. Mohammed, A.-J.; Maher, I.; Nakai, M.; Gepreel, M.A.H. Effects of cold rolling and heat treatment on the microstructure and hardness of pure aluminium. *Mater. Today Proc.* **2023**, doi:https://doi.org/10.1016/j.matpr.2023.09.138.
32. Conserva, M.; Donzelli, G.; Trippodo, R. *Aluminium and Its Applications*; Edimet, 1992; ISBN 9788886259019.
33. Davis, J.R. *Alloying: understanding the basics*; ASM international, 2001; ISBN 1615030638.

 doi:10.20944/preprints202408.1989.v1

34. Uscinowicz, R. The Effect of Rolling Direction on the Creep Process of Al–Cu Bimetallic Sheet. *Mater. Des.* **2013**, *49*, 693–700, doi:10.1016/j.matdes.2013.02.012.
35. Medjahed, A.; Moula, H.; Zegaoui, A.; Derradji, M.; Henniche, A.; Wu, R.; Hou, L.; Zhang, J.; Zhang, M. Influence of the Rolling Direction on the Microstructure, Mechanical, Anisotropy and Gamma Rays Shielding Properties of an Al-Cu-Li-Mg-X Alloy. *Mater. Sci. Eng. A. Struct. Mater.* **2018**, *732*, 129–137, doi:10.1016/j.msea.2018.06.074.
36. İriç, S.; Ayhan, A.O. Dependence of Fracture Toughness on Rolling Direction in Aluminium 7075 Alloys. *Acta Phys. Pol. A* **2017**, *132*, 892–895, doi:10.12693/APhysPolA.132.892.
37. Sakin, R. Investigation of bending fatigue-life of aluminum sheets based on rolling direction. *Alexandria Eng. J.* **2018**, *57*, 35–47, doi:https://doi.org/10.1016/j.aej.2016.11.005.
38. Wang, H. Effect of Rolling Direction to Texture Evolution in an Aluminium Single Crystal (011)[100]: A Crystal Plasticity FEM Investigation. *Mater. Res. express* **2019**, *6*, doi:10.1088/2053-1591/ab17b4.
39. Lv, F.; Yang, F.; Duan, Q.Q.; Luo, T.J.; Yang, Y.S.; Li, S.X.; Zhang, Z.F. Tensile and Low-Cycle Fatigue Properties of Mg–2.8% Al–1.1% Zn–0.4% Mn Alloy along the Transverse and Rolling Directions. *Scr. Mater.* **2009**, *61*, 887–890, doi:10.1016/j.scriptamat.2009.07.023.
40. Topic, I.; Höppel, H.W.; Göken, M. Influence of Rolling Direction on Strength and Ductility of Aluminium and Aluminium Alloys Produced by Accumulative Roll Bonding. *J. Mater. Sci.* **2008**, *43*, 7320–7325, doi:10.1007/s10853-008-2754-3.
41. Kazemi-Navaee, A.; Jamaati, R.; Aval, H.J. Asymmetric Cold Rolling of AA7075 Alloy: The Evolution of Microstructure, Crystallographic Texture, and Mechanical Properties. *Mater. Sci. Eng. A. Struct. Mater.* **2021**, *824*, doi:10.1016/j.msea.2021.141801.
42. Alves, L.M. Fracture Mechanics. *Prop. Patterns Behav.* 2016, 0–332.
43. Anderson, T.L.; Anderson, T.L. *Fracture mechanics: fundamentals and applications*; CRC press, 2005; ISBN 0429125674.
44. Jones, R.; Singh Raman, R.K.; McMillan, A.J. Crack growth: Does microstructure play a role? *Eng. Fract. Mech.* **2018**, *187*, 190–210, doi:https://doi.org/10.1016/j.engfracmech.2017.11.023.
45. Skallerud, B.; Iveland, T.; Härkegård, G. Fatigue life assessment of aluminum alloys with casting defects. *Eng. Fract. Mech.* **1993**, *44*, 857–874, doi:https://doi.org/10.1016/0013-7944(93)90108-5.
46. Zhu, X.-K.; Joyce, J.A. Review of fracture toughness (G, K, J, CTOD, CTOA) testing and standardization. *Eng. Fract. Mech.* **2012**, *85*, 1–46, doi:https://doi.org/10.1016/j.engfracmech.2012.02.001.
47. abu bakar, I. The Effect of Rolling Direction to the Tensile Properties of AA5083 Specimen. V; 2015; str. pp 779-787 ISBN 978-981-287-289-0.
48. Nazemi, N. Identification of the Mechanical Properties in the Heat-Affected Zone of Aluminum Welded Structures, ProQuest Dissertations Publishing, 2015.